



THE UNIVERSITY *of* EDINBURGH

Edinburgh Research Explorer

Dense SixGe_{1-x} (0 < x < 1) Materials Landscape Using Extreme Conditions and Precession Electron Diffraction

Citation for published version:

Serghiou, G, Ji, G, Koch-Mueller, M, Odling, N, Reichmann, HJ, Wright, JP & Johnson, P 2014, 'Dense SixGe_{1-x} (0 < x < 1) Materials Landscape Using Extreme Conditions and Precession Electron Diffraction', *Inorganic Chemistry*, vol. 53, no. 11, pp. 5656-5662. <https://doi.org/10.1021/ic500416s>

Digital Object Identifier (DOI):

[10.1021/ic500416s](https://doi.org/10.1021/ic500416s)

Link:

[Link to publication record in Edinburgh Research Explorer](#)

Document Version:

Peer reviewed version

Published In:

Inorganic Chemistry

General rights

Copyright for the publications made accessible via the Edinburgh Research Explorer is retained by the author(s) and / or other copyright owners and it is a condition of accessing these publications that users recognise and abide by the legal requirements associated with these rights.

Take down policy

The University of Edinburgh has made every reasonable effort to ensure that Edinburgh Research Explorer content complies with UK legislation. If you believe that the public display of this file breaches copyright please contact openaccess@ed.ac.uk providing details, and we will remove access to the work immediately and investigate your claim.



A dense $\text{Si}_x\text{Ge}_{1-x}$ ($0 < x < 1$) materials landscape using extreme conditions and precession electron diffraction

George Serghiou,^{1} Gang Ji,² Monika Koch-Müller,³ Nicholas Odling,⁴ Hans J. Reichmann,³ Jonathan P Wright,⁵ and Paul Johnson^{1#}*

¹University of Edinburgh, School of Engineering and Centre for Materials Science, Kings Buildings,
Mayfield Road, EH9 3JL Edinburgh, UK

²Unité Matériaux et Transformations, UMR CNRS 8207, Université Lille 1, Villeneuve d'Ascq,
59655 Lille, France

³Helmholtz Centre Potsdam, German Research Centre for Geosciences, Telegrafenberg, 14473 Potsdam,
Germany

⁴University of Edinburgh, School of Geosciences, The Grant Institute, Kings Buildings, West Mains
Road, EH9 3JW Edinburgh, UK

⁵European Synchrotron Radiation Facility, F-38043 Grenoble, France

[#]Present address: Safetec UK Limited, 16 Albert Street, Aberdeen, AB25 1XQ (UK)

*Author to whom correspondence should be addressed: george.serghiou@ed.ac.uk

RECEIVED DATE

Abstract

High pressure and temperature experiments on Ge and Si mixtures to 17 GPa and 1500 K allow us to obtain extended Ge-Si solid solutions with cubic ($Ia\bar{3}$) and tetragonal ($P4_32_12$) crystal symmetries at ambient pressure. The cubic modification can be obtained with up to 77 atomic percent Ge, and the tetragonal modification for Ge concentrations above that. Together with Hume-Rothery criteria, melting point convergence is employed here as a favoured attribute for solid solution formation. These compositionally tunable alloys are of growing interest for advanced transport and optoelectronic applications. Furthermore, the work illustrates the significance of employing precession electron diffraction for mapping new materials landscapes resulting from tailored high pressure and temperature syntheses.

Introduction

While cubic diamond-structured silicon is the single most important material in the semiconductor industry, it has an indirect band gap¹ and a fixed lattice constant, constraining it from efficient light emitting applications including most prominently photovoltaics and laser devices. This constraint remains present for its associated cubic diamond-structured pure germanium¹ and silicon-germanium alloy² counterparts because they also retain fundamental indirect band-gaps. There is a strong drive however to extend the functionality of (Si, Ge)-based technology from microelectronics into optoelectronics. This has led to investigation of a number of avenues, all based on processing of cubic diamond-structured (Si, Ge), to address this constraint.^{3,4} These avenues include doping silicon with erbium to serve as a lasing centre⁵, etching silicon with hydrogen fluoride to create pores resulting in luminescence due to quantum confinement effects⁶, inducing tensile strain coupled with n-type doping in germanium to access direct-gap emission in the indirect gap material⁷ and hybrid approaches⁸ interfacing silicon with other light emitting chemical compounds.

Our approach is different. Rather than process the existing cubic diamond structure that does not intrinsically exhibit targeted properties, transform it instead to a different crystal symmetry that does. That is, develop a new $\text{Si}_{1-x}\text{Ge}_x$ materials landscape by exploring synthesis of new structures which intrinsically contain tunable properties including fundamental direct band-gaps. To evaluate optimal pressure and temperature regions for novel solid solution formation, we examine the phase relations of the two endmembers, Si and Ge.^{9,10} Si and Ge are both semiconductors with the cubic diamond structure up to about 10 and 12 GPa respectively.¹¹ Hence synthesis within this pressure regime will only allow us to obtain the known cubic diamond structured semiconducting SiGe equilibrium modification.¹² Above about 12 GPa however, the endmembers are both metallic, having transformed to the β -Sn modification.^{11,13} Ge retains this modification up to 75 GPa^{14,15} whereas Si undergoes several phase transitions: above 13 GPa^{16,17} it transforms to an orthorhombic phase, to a simple hexagonal phase above 15 GPa^{16,17}, to another orthorhombic phase above 38 GPa¹⁸, and to a hexagonal close packed phase above 42 GPa¹⁹ (Figure 1). Hence between 12 and 13 GPa all four generally accepted criteria for

solid solution formation, namely same crystal structure, atomic radii ratios within 15% of each other, similar valencies and electronegativities are fulfilled.²⁰

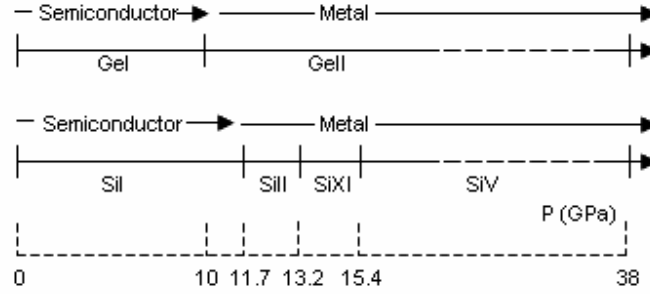


Figure 1. Comparison of the pressure-induced structural transitions of Ge and Si upon room temperature compression to 38 GPa. Semiconducting GeI (cubic diamond structure, $Fd\bar{3}m$) transforms to metallic GeII (β -Sn structure ($I4_1/amd$)) above 9 GPa. This structure is retained to 45 GPa. Semiconducting SiI (cubic diamond structure $Fd\bar{3}m$) transforms to metallic SiII (β -Sn structure ($I4_1/amd$)) above 11 GPa. Above 13 GPa, this phase transforms to an orthorhombic ($Imma$) modification, to a hexagonal modification (P_6/mmm) above 15 GPa, another orthorhombic phase ($Cmca$) above 38 GPa, and a further hexagonal modification ($P6_3/mmc$) above 42 GPa.

This is not to say that at higher pressures synthesis of SiGe is not merited. While, the crystal structures are indeed no longer the same, the atomic radii ratios are still within about 6% of each other and the electronic properties remain compatible (Figures 1, 2). Furthermore, the melting points are virtually identical at 17 GPa which serves as an additional barrier against segregation (Figure 3). Contrastingly²⁹, at ambient pressure, despite the four criteria for solid solution being formally fulfilled, the more than 500 K melting point difference between Si and Ge, leads in actuality, to profound segregation effects. This makes extended homogeneous solid solution formation, extremely difficult,³⁰ especially on the germanium-rich side, due to the larger segregation coefficients for germanium-rich compositions.^{31,32} The impetus for synthesis, and promise of obtaining technologically important, tunable novel solid solutions is reinforced by a host of recent experiments and calculations on preparation, stability and optoelectronic properties of Si and Ge phases.³³⁻⁴² Pure Ge obtained at ambient pressure from above 10-

12 GPa is tetragonal ($P4_32_12$)⁴³ and calculated to exhibit a direct-band gap.⁴⁴

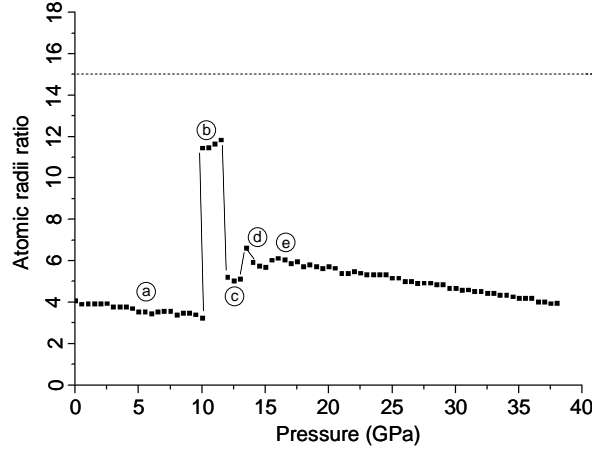


Figure 2. Ge-Si atomic radii ratio (% difference) pressure dependence from ambient to 38 GPa. Points a through e reveal respectively the ratios between GeI ($Fd\bar{3}m$) and SiI, GeII ($I4_1/amd$) and SiI ($Fd\bar{3}m$), GeII and SiII ($I4_1/amd$), GeII and SiXI ($Imma$) and GeII and SiV (P_6/mmm).^{19,21-25} The dashed line depicts the Hume-Rothery tolerance atomic radius ratio boundary below which solid solution formation is favored.

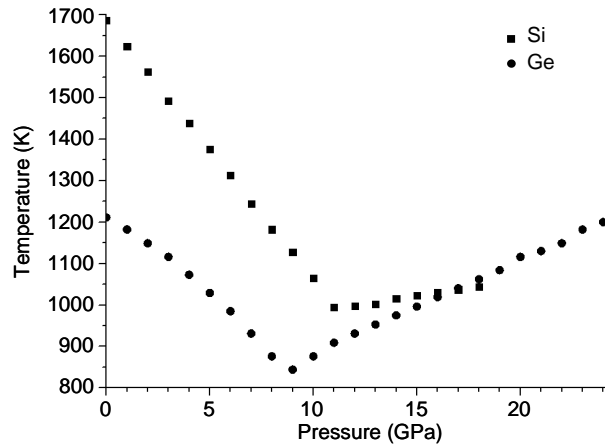


Figure 3. Pressure dependency of the melting points of Ge and Si.^{9, 26-28} The negative melting slopes for both elements is due to the higher density of their liquid states which are metallic, unlike their solid states which are semiconducting in the cubic diamond phase. On transition to metallic crystal structures at higher pressures the melting slopes become positive. In the pressure regime of our experiments the melting points of Ge and Si converge.

Hence a Ge-rich tetragonal GeSi solid solution should exhibit a tunable direct band-gap.⁴⁵ Furthermore,

Si with the $P4_32_12$ tetragonal modification could upon doping exhibit a higher superconducting temperature than those of the other Si-modifications.⁴⁶ While Si does not form this tetragonal phase, targeted solid solution with Ge, which does, could then lead to a bulk Si-based tetragonal phase with elevated superconducting T_c upon doping. Additionally, pure Si obtained at ambient conditions from above 12-13 GPa is cubic ($Ia\bar{3}$) and is a semi-metal.^{43,44} Thus Si solid solution with Ge within a complementary compositional range to that stabilizing a $P4_32_12$ phase, can result in a compositionally tunable SiGe cubic ($Ia\bar{3}$) phase, which upon crystal size tuning may, due to multiple exciton generation and optimized band gap, be considered for solar conversion applications.³⁹ A disordered hexagonal phase (2H lonsdaleite)^{47,48} for both Ge and Si has also been obtained at 1 atm from above 10 GPa for both Ge and Si. We perform hence here synthesis experiments at pressures between 12 to 17 GPa coupled with electron microscopy and synchrotron characterization experiments on a series of Ge and Si starting mixtures targeting new alloys in this system with tunable structure and properties.

Experimental section

We employed ultrapure Ge pieces (99.9999+% puratronic Alfa Aesar) and Si pieces (99.999 metal basis % Alfa Aesar) as starting materials. The high pressure experiments were performed at the German Research Centre for Geosciences in Potsdam. Seven multi-anvil experiments on Ge:Si mixtures placed in lidded aluminum oxide crucibles were performed, three at 12 GPa, two at 13 GPa and two at 17 GPa. For the experiments at relatively low pressure (12 and 13 GPa) 14/8 assemblies (octahedral length/truncation length) were used with a MgO-based octahedron serving as a pressure transmitting medium. Details of the experimental setup are given in (49). The 17 GPa experiments were performed with a 10/5-assembly, which was calibrated using the following phase transitions: coesite-stishovite⁵⁰, α - β Mg_2SiO_4 ⁵¹, β - γ Mg_2SiO_4 ⁵², enstatite- β - Mg_2SiO_4 -stishovite⁵³. In all experiments stepped graphite heaters were employed and temperatures were measured with type C thermocouples ($W_{50}Re/W_{26}Re$), with electromotive forces uncorrected for pressure.

At 12 GPa 80:20, 50:50 and 20:80 at% Ge:Si mixtures respectively were melted at 1500 K for 2 minutes followed by annealing at 650 K for 1 hour before temperature and then pressure quenching. At

13 GPa 75:25 and 40:60 at% Ge:Si mixtures respectively were melted at 1500 K for 2 minutes followed by annealing at 650 K for 2 hours before temperature and then pressure quenching. At 17 GPa 75:25 and 60:40 at% Ge:Si mixtures respectively were melted at 1500 K for 2 minutes followed by annealing at 800 K for 2 hours before temperature and then pressure quenching.

The samples were polished and carbon coated for electron microscopy measurements. Scanning Electron Microscopy (Philips XL30CP), with an Energy Dispersive X-ray (EDX) analyser (Oxford instruments EDX detector – SiLi crystal with PGT spirit analysis software) was employed for chemical and morphological analysis from the polished pellets. The acceleration voltage used was set to 20 kV. Backscattered electron mode was primarily used because it allows for chemical contrast.^{54,55} Samples were also investigated with a Philips CM30, Transmission Electron Microscope (TEM), equipped with a 1k x 1k Gatan slow scan CCD camera and with Digital Micrograph software for acquisition of electron diffraction patterns and bright-field imaging with an accelerating voltage of 300 kV. A double tilting stage allowed us to record multiple zone-axes patterns from single crystals. The CM30 is also equipped with a Nanomegas “Spinning Star” precession system and a Noran EDX detector for local chemical analysis. The camera length for TEM was calibrated using pure silicon. Semi-quantitative chemical analysis was carried out without standards for the determination of the Cliff-Lorimer factors and without measurement of local thin foil thickness. Precession electron diffraction (PED) measurements were performed in microdiffraction mode, i.e. with a nearly parallel incident beam focused on the specimen with a spot size in the range of 10 to 50 nm. The precession semi-angle of 2° was set to record PED patterns. The maximum precession angle of about 3° was systematically used in order to further identify the kinematically forbidden reflections.⁵⁶⁻⁵⁸ PED performed at a high precession semi-angle of $\geq 2^\circ$ in particular, significantly reduces the overall dynamical effects involved in an electron diffraction pattern, which in turn allows for a drastically improved measurement of kinematical intensities of diffracted reflections from the single crystallites. This facilitates differentiation even between closely related diffraction patterns and concomitant accurate crystallographic indexing of the new phases.⁵⁶⁻⁶³ Supporting angle dispersive X-ray diffraction measurements were performed at the ID11 beamline of

the European Synchrotron Radiation Facility. A monochromatic X-ray beam ($\lambda = 0.31849 \text{ \AA}$) was focused to $10 \text{ \mu m} \times 7 \text{ \mu m}$ using a tunable X-ray focusing apparatus (transfocator) containing twenty beryllium lenses and 254 aluminium lenses.⁶⁴ A Frelon 4M CCD detector was used for diffraction data collection with a pixel size of $50 \times 50 \text{ \mu m}$. LaB_6 powder (National Institute of Standards SRM 660a), also placed in a square on a copper grid and on kapton holders, was used to calibrate the distance and orientation of the detector. A Si-fluorescence detector was also installed on ID11 which allowed us to obtain a chemical signature from the very spot from which diffraction was performed. The crystal sizes observed with electron microscopy ranged from about 50 nanometres to a few microns. The combination of PED/EM and XRD allows for highly spatially resolved structural and chemical analysis together with high angular resolution structural analysis. When characterizing small single crystals, and/or a heterogeneous assembly, electron diffraction, is particularly needed. For the electron and X-ray diffraction measurements, particles of the reaction product from the polished half capsules were taken under an 126x total magnification optical microscope, using a sharp tungsten carbide needle and dispersed onto the thin carbon film of labelled three millimeter diameter copper TEM grids (Agar scientific). For the X-ray diffraction measurements, particles were placed on litholoops (Molecular Dimensions Limited) as well. For the litholoops, typically used for larger sample amounts, the principal advantage is the absence of any crystalline features (e.g. Cu in a grid) whose signal may interfere with sample patterns. Thus one can freely rotate the litholoop about its axis, to obtain better powder averaging and minimize any texturing effects. Based on numerous comparative measurements, we found that the signal to noise ratio of diffraction peaks of material placed on the TEM grid is typically about a factor of 2 higher than that from the litholoop. This may be attributed to the carbon foil of the TEM grid being more than two orders of magnitude thinner than the litholoop's rigid kapton foil (holes on the litholoop are typically too large for the small samples). Further beneficial attributes of the TEM grid are the greater ease in locating and aligning the sample with the beam because the sample is framed by the copper grid and the better adherence of the material to the carbon foil. Equally, even with typically 45 degree rotation applied, the spatial resolution with a small beam spot sufficed, in avoiding copper

diffraction peaks. Use of the TEM grid, means that one can formally examine the same sample as was examined with TEM, which is particularly important for obtaining multifaceted complementary structural, chemical and morphological information, particularly from precious material. The zone-axis electron diffraction patterns were interpreted using the software “Electron Diffraction” version 7.01 by considering the kinematical approximation.⁶⁵ Note that in all the simulated zone-axis diffraction patterns shown hereafter an empty circle represents a kinematically forbidden reflection and the size of a filled circle is proportional to the intensity of the diffracted reflection. The X-ray diffraction patterns were circularly integrated using Fit2D⁶⁶ and the one-dimensional patterns were fitted and indexed using the Topas 3.0 software.⁶⁷ The chemical signatures taken from the samples at ID11 in-parallel with the diffraction, was performed using the program PyMCA.⁶⁸

Results

PED analysis of numerous single crystallites with accompanying chemical analysis from each analyzed crystallite from the obtained products allowed us to develop a structure- composition map of the reaction products. We present examples documenting the $Ia\bar{3}$ assignment first, followed by examples documenting the $P4_32_12$ assignment and finally examples of our chemical analysis of crystals from both symmetries. Figure 4 shows representative zone-axis PED diffraction patterns of the Ge-Si crystallites obtained with $Ia\bar{3}$ symmetry (Figures 4a, c) together with their simulated diffraction patterns (Figures 4b, d) revealing the excellent match with the experimental data. A further

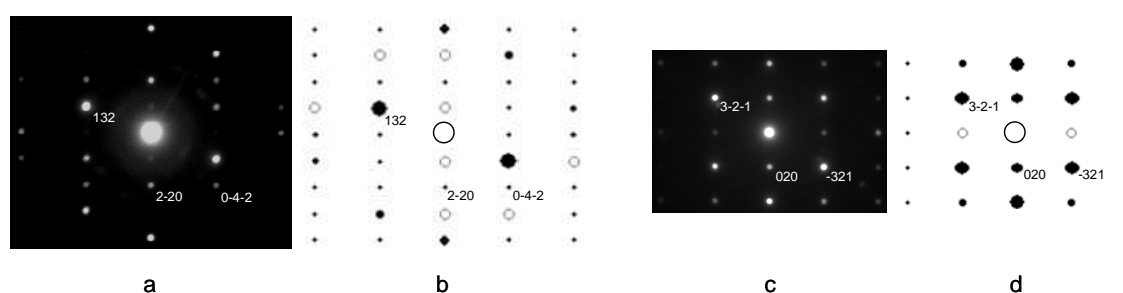


Figure 4. Experimental PED and simulated zone-axis diffraction patterns of binary Ge-Si crystals with $Ia\bar{3}$ space group. (a, b) are experimental and simulated zone-axis diffraction patterns of the $[11\bar{2}]$ zone axis and (c, d) correspondingly, of the $[103]$ zone-axis.

Ge-Si experimental zone-axis PED pattern (Figure 5a) is compared with its corresponding simulated $Ia\bar{3}$ (Figure 5b) and its site ordered $Pa\bar{3}$ symmetry analogue (Figure 5c), revealing that our

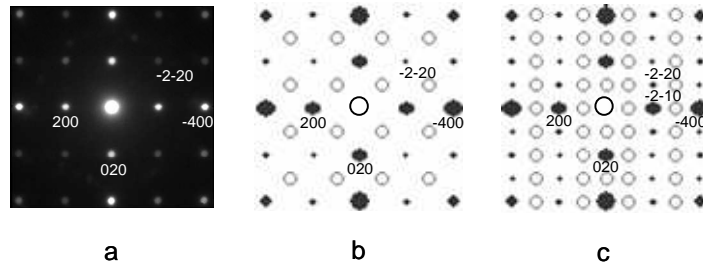


Figure 5. Comparison of an experimental zone-axis PED pattern of a binary Ge-Si crystal to simulated ones, without ($Ia\bar{3}$) and with ($Pa\bar{3}$) site-ordering. (a) Experimental precession electron diffraction $[001]$ zone-axis pattern and simulated $[001]$ zone-axes with (b) $Ia\bar{3}$ and (c) $Pa\bar{3}$ space groups.

new cubic binary Ge-Si phase exhibits no long range site-ordering. The importance of PED for unambiguous indexing of the $Ia\bar{3}$ space group is further illustrated in figure 6 by comparing an experimental zone axis diffraction pattern taken without, (Figure 6a) and with (Figure 6c) precession to that of the corresponding simulated pattern (Figure 6b). Figure 7 shows representative

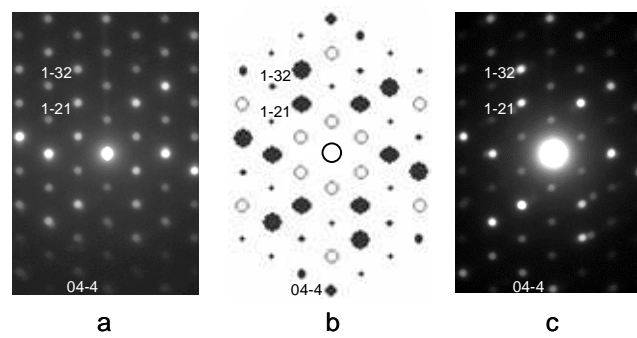


Figure 6. (a, c) Experimental [111] zone-axis electron diffraction pattern for a binary Ge-Si crystal with $Ia\bar{3}$ space group measured without and with precession and a (b) simulated [111] zone-axis pattern.

zone-axis diffraction patterns of the Ge-Si crystallites obtained with $P4_32_12$ symmetry (Figures 7a, c) together with their simulated diffraction patterns (Figures 7b, d) revealing the excellent match with the

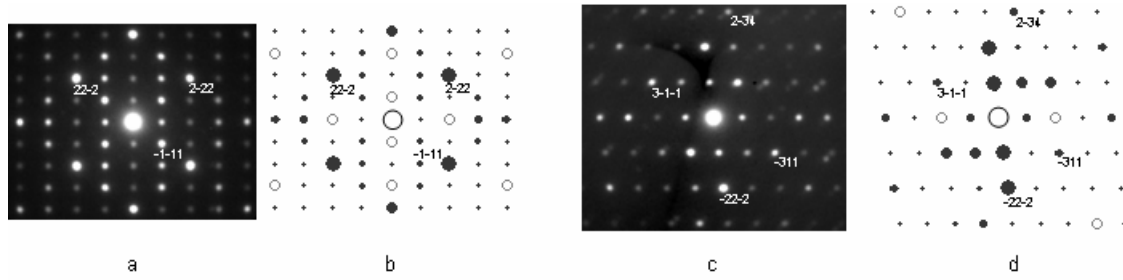


Figure 7. Experimental PED and simulated zone-axis diffraction patterns of binary Ge-Si crystals with $P4_32_12$ space group. (a, b) are experimental and simulated zone-axis diffraction patterns of the [011] zone axis and (c, d) correspondingly, of the [121] zone-axis.

experimental data. Unlike the cubic modification, consideration of a site-ordered analogue is not merited because it does not occur for the tetragonal phase.⁶⁹ The importance of PED for unambiguous indexing of the $P4_32_12$ space group, is further illustrated in figure 8 by comparing an experimental zone-axis diffraction pattern taken without, (Figure 8a) and with (Figure 8c) precession to that of the corresponding simulated pattern (Figure 8b). The $Ia\bar{3}$ symmetry occurs for compositions from 100 to

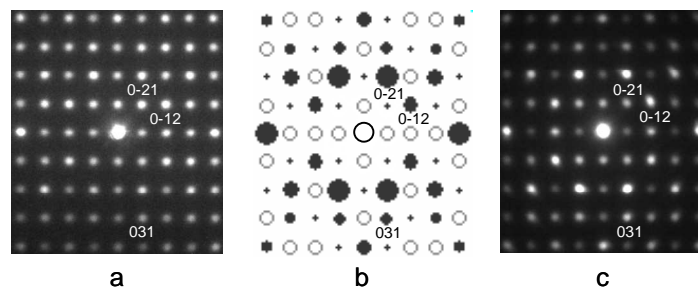


Figure 8. (a, c) Experimental [100] zone-axis electron diffraction pattern for a binary Ge-Si crystal with $P4_32_12$ space group measured without and with precession and (b) a simulated [100] zone-axis pattern.

about 23 at.% Si, with the $P4_32_12$ symmetry occurring for Si compositions from 22 at% Si downwards. Examples of chemical analysis taken from crystallites of both symmetries are shown in Figures 9a-c.

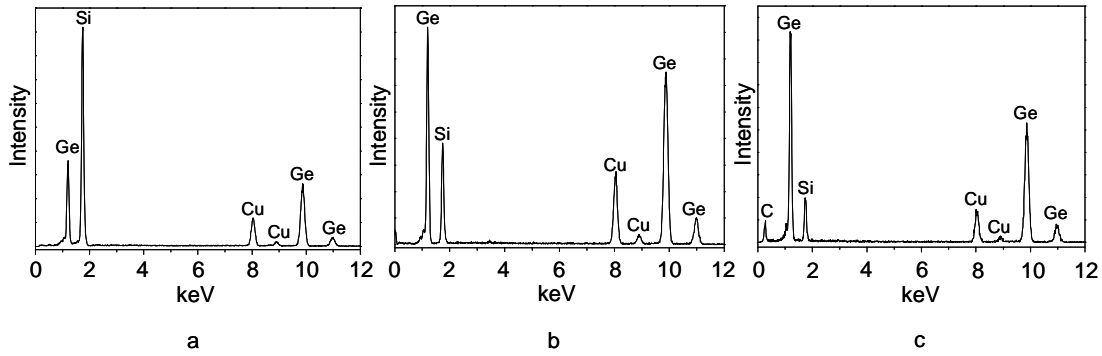


Figure 9. Examples of TEM/EDX chemical analysis from Ge-Si crystals obtained at ambient conditions after high pressure and temperature syntheses. (a, b) Semi-quantitative energy dispersive X-ray analysis from two crystals with $Ia\bar{3}$ space group revealing $\text{Ge}_{0.25}\text{Si}_{0.75}$ and $\text{Ge}_{0.65}\text{Si}_{0.35}$ stoichiometries respectively, and one (c) with $P4_32_12$ space group revealing a $\text{Ge}_{0.81}\text{Si}_{0.19}$ stoichiometry. The C and Cu peaks originate respectively, from the carbon foil and the copper grid of the TEM sample holder.

The only other highly crystalline symmetry detected from a few crystallites after release from 12 GPa, was the ambient pressure cubic diamond symmetry likely because this pressure may be close to the transition pressure between SiGe cubic diamond and the β -Sn modification.⁷⁰⁻⁷⁵ Disordered structures with hexagonal symmetry, likely with varying polytypic characteristics, for a range of Ge-Si compositions were however also detected here from all pressures. These were more prevalent as the Ge content increased. Indeed their enhanced presence in the reaction product matrix for Ge-rich compositions has hindered us so far from obtaining an accompanying X-ray diffraction pattern of Ge-Si with $P4_32_12$ symmetry and will be the focus of a further report. Angle dispersive X-ray diffraction

measurements on the other hand, from binary $Ia\bar{3}$ Si-rich compositions were obtained. An X-ray diffraction pattern from a sample extracted from a pellet which has a bulk 20:80 Ge:Si composition, based on chemical analysis using scanning electron microscopy, is shown in Figure 10.

Discussion

We provide here an explanation for the composition-structure relationship measured and why in particular the binary Ge-Si cubic $Ia\bar{3}$ phase is obtained for a larger range of Ge-Si compositions than the $P4_32_12$ phase is. With respect to compression of Ge and Si (Figure 1), differences upon release from 17 GPa are that, GeII transforms to $P4_32_12$ below about 9 GPa and is retained at 1 atm, and SiII transforms to an $R\bar{3}$ phase below about 9 GPa, before $Ia\bar{3}$ is obtained below 2 GPa and retained at 1 atm.^{10,43} The Si $Ia\bar{3}$ and Ge $P4_32_12$ phases are stable indefinitely at ambient conditions.

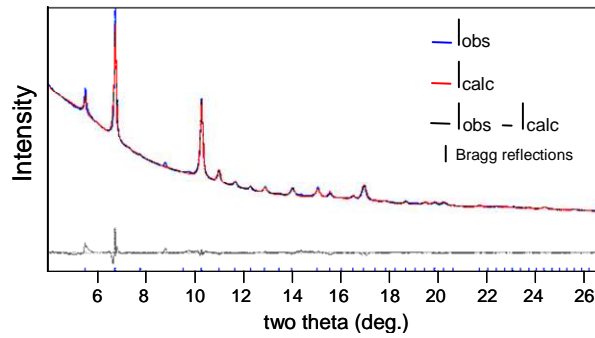


Figure 10. A X-ray diffraction pattern of a $\text{Ge}_{0.2}\text{Si}_{0.8}$ composition with $Ia\bar{3}$ space group ($a = 6.676$ (1) Å) and a calculated density of $\rho = 3.303 \text{ g/cm}^3$. We have to-date also measured the X-ray diffraction pattern of a $\text{Ge}_{0.5}\text{Si}_{0.5}$ composition with $Ia\bar{3}$ space group ($a = 6.782$ (1) Å) and a calculated density of $\rho = 4.287 \text{ g/cm}^3$. For reference the corresponding densities of cubic diamond $Fd\bar{3}m$ $\text{Ge}_{0.2}\text{Si}_{0.8}$ and $\text{Ge}_{0.5}\text{Si}_{0.5}$ are respectively $\rho = 2.998 \text{ g/cm}^3$ and $\rho = 3.938 \text{ g/cm}^3$.¹²

These crystal structures, rather than the cubic diamond structure, are obtained, because they are kinetically accessible from denser phases upon release.⁷⁶ Indeed, even intermediate heating experiments on Si $Ia\bar{3}$ result in a hexagonal ($P6_3mc$ 2H) rather than the diamond phase because the bond reconstruction required for the latter is too severe.^{43,47} The internal energies of the $P4_32_12$ and $Ia\bar{3}$

phases are very similar.^{44,77} Why Ge favors $P4_32_12$, while Si favours the $Ia\bar{3}$ phase can be explained from a structural point of view.^{44,69} Ge $P4_32_12$ and Si $Ia\bar{3}$ are comprised of tetrahedral units, as is their lowest energy, but kinetically inaccessible cubic diamond $Fd\bar{3}m$ counterpart. In $Fd\bar{3}m$ Ge and Si, the tetrahedra are undistorted and characterized by a single bond length. Deviation from this structure by $P4_32_12$ and $Ia\bar{3}$ has two energetic penalties, one, the degree of tetrahedral bond angle distortion and two, the degree of deviation from the diamond $Fd\bar{3}m$ bond length. $P4_32_12$ allows for a greater proximity of its bond lengths to that of $Fd\bar{3}m$ at the cost of greater tetrahedral bond angle distortions. Conversely, $Ia\bar{3}$, allows for smaller tetrahedral bond angle distortions at the cost of greater deviation of the bond lengths from those in the $Fd\bar{3}m$ diamond phase.⁷⁷ Ge adopts the $P4_32_12$ structure because the Ge bonds are less stiff than those of Si (vibrational frequencies are lower than in Si). Hence its structure can accommodate greater angular distortions with relative ease, benefiting on the other hand from bond lengths closer to those of $Fd\bar{3}m$ diamond. The Si bonds on the other hand are stiff, requiring the structure to remain relatively undistorted, at the expense however, of a greater distribution of bond lengths with respect to those in $Fd\bar{3}m$ diamond. Despite their very similar energies, the $Ia\bar{3}$ symmetry may be viewed as slightly favored based on the additional observation that the $P4_32_12$ symmetry is not accessible for endmember Si, whereas the $Ia\bar{3}$ symmetry can be accessed by Ge under rapid pressure release, albeit fleetingly, with ensuing transition to a hexagonal ($P6_3mc$ 2H) phase.⁷⁸

Another reason that the $Ia\bar{3}$ symmetry may be compositionally more favoured, even for same group members, is because of an energetic cost to having same element nearest neighbours.^{10,69} While group IV binaries with $P4_32_12$ ⁷⁹ and $Ia\bar{3}$ symmetries (Figure 5) both adopt structures without long range site-ordering, only the $Ia\bar{3}$ symmetry has an equivalent site-ordered $Pa\bar{3}$ description⁸⁰ which allows nearest neighbours to be of the second element. $P4_32_12$ does not have this option, because unlike $Ia\bar{3}$, it contains rings with odd numbers of atoms.^{10,69,81} Hence local level site ordering¹⁰ to alleviate any residual strain is only favored for the $Ia\bar{3}$ symmetry. These considerations provide an explanation for

why, within this newly established SiGe materials landscape, the $Ia\bar{3}$ symmetry spans a wider range of compositions than the $P4_32_12$ symmetry does.

Conclusions

The combination of high pressures and temperatures has allowed us to form a materials landscape for $\text{Ge}_x\text{Si}_{1-x}$ $0 < x < 1$ containing tetragonal $P4_32_12$ and cubic $Ia\bar{3}$ symmetries, with projected electronic character ranging from semiconducting to semi-metallic, of optoelectronic, transport and thermoelectric interest.^{39, 46} Further, Ge-Si alloying, in addition to providing tunability of properties can also contribute to greater structural stability. For example, Ge alloys with tetragonal symmetry exhibit enhanced cycling performance as battery anodes.⁴⁰ The work here also includes the first participation of Si in a $P4_32_12$ alloy and together with the new phase relations in Ge-Sn^{79,82,83} paves the way for even greater tunability in novel ternary Si-Ge-Sn systems. The work also reveals the effectiveness of linking, together with X-rays, PED with extreme conditions for creation and characterization of new materials landscapes. This highest possible spatially resolved detection of new single crystallites and their distinct structural analysis based on both spot positional distribution and kinematical intensity profile markedly limits ambiguity of assignment and facilitates confident advance.

Acknowledgments

We are grateful to Professor Jean-Paul Morniroli for his guidance and support. The TEM facility in Lille (France) is supported by the Conseil Regional du Nord-Pas de Calais and the European Regional Development Fund (ERDF). We also acknowledge EU proposal MA712 for experiments at ESRF (European Radiation Synchrotron Facility). We also thank the Moray foundation and the Innovative Initiative grant program for support. We further warmly thank Ahmed Addad for his work and consultation on chemical microanalysis using transmission electron microscopy, Nicola Cayzer for consultation on scanning electron microscopy, Michael Hall for demanding solids processing, and Mark Gibbard for some data processing. We also thank Reiner Schulz and Andreas Ebert for their support during the multi-anvil experiments.

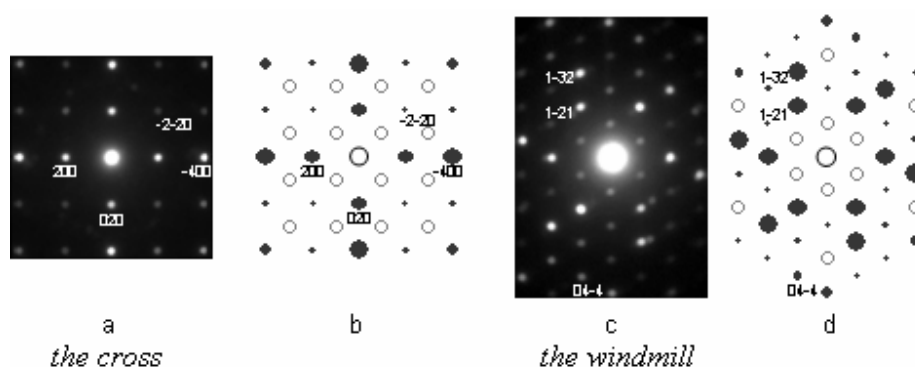
References

- (1) Hybertsen, M. S.; Louie, S. G. *Phys. Rev. B* **1986**, *34*, 5390-5413.
- (2) Braunstein, R.; Moore, A. R.; Herman, F. *Phys. Rev. B* **1958**, *109*, 695-710.
- (3) Cloutier, S. G.; Kossyrev, P.A.; Xu, J. *Nat. Mat.* **2005**, *4*, 887-891.
- (4) Kuo, Y. H.; Lee, Y. K.; Ge, Y. S.; Ren, S.; Roth, J. E.; Kamins, T.I.; Miller, D. A. B.; Harris, J. S. *Nature* **2005**, *437*, 1334-1336.
- (5) Vinh, N. Q.; Ha, N. N.; Gregorkiewicz, T. *Proc. of the IEEE* **2009**, *97*, 1269-1283.
- (6) Adachi, S.; Oi, M. *J. Appl. Phys.* **2007**, *102*, 063506-063515.
- (7) Liu, J.; Sun, X.; Pan, D.; Wang, X.; Kimerling, L. C.; Koch, T. L.; Michel, J. *Opt. Expr.* **2007**, *15*, 11272-11277.
- (8) Vasdekis, A. E.; Moore, S. A.; Ruseckas, A.; Krauss, T. F.; Samuel, I. D. W.; Turnbull, G. A. *Appl. Phys. Lett.* **2007**, *91*, 051124-051127.
- (9) Young, D. A. *Phase Diagrams of the Elements*; 1st ed.; University of California Press: Berkeley, 1991.
- (10) Mujica, A; Rubio, A; Munoz, A; Needs, R. J. *Rev. Mod. Phys.* **2003**, *75*, 863-912.
- (11) Bundy, F. P. *J. Chem. Phys.* **1964**, *41*, 3809-3814.
- (12) Dismukes, J. P.; Paff, R. J.; Ekstrom, L. *J. Phys. Chem.* **1964**, *68*, 3021-3027.
- (13) Jamieson, J. C. *Science* **1963**, *139*, 762-764.
- (14) Vohra, Y. K.; Brister, K. E.; Desrgeniers, S; Ruoff, A. L.; Chang, K. J.; Cohen, M. L. *Phys. Rev. Lett.* **1986**, *56*, 1944-1947.
- (15) Nelmes, R. J.; Liu, H; Belmonte, S. A.; Loveday, J. S.; McMahon, M. I.; Allan, D. R.; Hausermann, D.; Hanfland, M. *Phys. Rev. B* **1996**, *53*, R2907-R2909.
- (16) McMahon, M. I.; Nelmes, R. J; Wright, N. G.; Allan, D. R. *Phys. Rev. B* **1994**, *50*, 739-743.
- (17) Lewis, S. P.; Cohen, M. L. *Phys. Rev. B* **1993**, *48*, 16144-16147.
- (18) Hanfland, M; Schwarz, U; Syassen, K.; Takemura, K. *Phys. Rev. Lett.* **1999**, *82*, 1197-1200.
- (19) Hu, J. Z.; Merkle, L. D.; Menoni, C. S.; Spain, I. L. *Phys. Rev. B* **1986**, *34*, 4679-4684.
- (20) Hume-Rothery, W.; Smallman, R. E.; Haworth, C. W. *The Structure of Metals and Alloys*; 5th ed.; The Chaucer Press: London, 1969.
- (21) Chang, K. J.; Cohen, M. L. *Phys. Rev. B* **1986**, *34*, 8581-8590.
- (22) Di Cicco, A.; Frasini, A. C.; Minicucci, M.; Principi, E.; Itie, J. P.; Munsch, P. *Phys. Stat. Solidi B-Basic Res.* **2003**, *240*, 19-28.
- (23) Mckimin, H. J.; Andreatch, P. *J. Appl. Phys.* **1964**, *35*, 2161-2165.
- (24) McMahon, M.I.; Nelmes, R. J.; Wright, N. G.; Allan, D. R. *Phys. Rev. B* **1994**, *50*, 739-743.
- (25) Gaal-Nagy, K; Strauch, D. *Comput. Mat. Sci.* **2004**, *30*, 8-15.
- (26) Prakapenka, V.; Kubo, A.; Kuznetsov, A.; Laskin, A.; Shkurikhin, O.; Dera, P.; Rivers, M. L.; Sutton, S. R. *High Pressure Res.* **2008**, *28*, 225-235.
- (27) Kubo, A.; Wang, Y.; Runge, C. E.; Uchida, T.; Kiefer, B.; Nishiyama, N.; Duffy, T. S. *J. Phys. Chem. Solids* **2008**, *69*, 2255-2260.
- (28) Voronin, G. A.; Pantea, C.; Zerda, T. W.; Zhang, J.; Wang, L.; Zhao, Y. *J. Phys. Chem. Solids* **2005**, *64*, 2113-2119.
- (29) Serghiou, G.; Odling, N.; Hunter R.; Abbie, A; Armstrong, B.; Lathe, C. *High Pressure Res.* **2014**, *34* in press.
- (30) Schilz, J.; Romanenko, V. N. *J. Mat. Sci.-Mat. Electr.* **1995**, *6*, 265-279.
- (31) Dario, A.; Sicim, A. O.; Balicki, E. *J. Cryst. Growth* **2011**, *337*, 65-71.
- (32) Kostylev, I.; Woodacre, J. K.; Lee, Y. P.; Klages, P.; Labrie, D. J. *Cryst. Growth* **2013**, *377*, 147-152.
- (33) Zhang, P. H.; Crespi, V.H.; Chang, E.; Louie, S. G.; Cohen, M. L. *Nature* **2001**, *409*, 69-71.

- (34) Botti, S.; Flores-Livas, J. A.; Amsler, M.; Goedecker, S.; Marques, M. A. L. *Phys. Rev. B* **2012**, *86*, 121204-121209.
- (35) Malone, B. D.; Louie, S. G.; Cohen, M. L. *Phys. Rev. B* **2010**, *81*, 115201-115206.
- (36) Kim, S. J.; Quy, O. K.; Chang, Ling-Shao; Stach, E. A.; Handwerker, C. A.; Wei, A. *J. Mat. Chem.* **2010**, *20*, 331-337.
- (37) Sato, S.; Nozaki, S.; Morisaki, H. *Appl. Phys. Lett.* **1998**, *72*, 2460-2462.
- (38) Selli, D.; Boulfelfel, S. E.; Baburin, I. A.; Seifert, G.; Leoni, S. *RSC Adv.* **2012**, *2*, 8833-8839.
- (39) Wippermann, S.; Voeroes, M.; Rocca, D.; Gali, A.; Zimanyi, G.; Galli, G. *Phys. Rev. Lett.* **2013**, *110*, 046804-046809.
- (40) Cho, Y. J.; Im, H. S.; Kim, H. S.; Myung, Y.; Back, S. H.; Lim, Y. R.; Jung, C. S.; Jang, D. M.; Park, J.; Cha, E. H.; Il Cho, W.; Shojaei, F.; Kang, H. S. *ACS NANO* **2013**, *7*, 9075-9084.
- (41) Johnson, B. C.; Haberl, B.; Deshmukh, S.; Malone, B. D.; Cohen, M. L.; McCallum, J. C.; Williams, J. S.; Bradby, J. E. *Phys. Rev. Lett.* **2013**, *110*, 085502-085507.
- (42) Xiang, H. J.; Huang, B.; Kan, E.; Wei, S. H.; Gong, X. G. *Phys. Rev. Lett.* **2013**, *110*, 118702-118706.
- (43) Kasper, J. S.; Richards, S. M. *Acta Crystallogr.* **1964**, *17*, 752-755.
- (44) Mujica, A.; Needs, R. J. *Phys. Rev. B* **1993**, *48*, 17010-17017.
- (45) Bottomley, D. J.; Delaunay, J.J.; Tomita, M.; Hayashi, T. *Thin Solid Films* **2002**, *402*, 143-153.
- (46) Malone, B. D.; Sau, J. D.; Cohen, M. L. *Phys. Rev. B* **2008**, *78*, 035210-035217.
- (47) Wentorf, R. H.; Kasper, J. S. *Science* **1963**, *139*, 338-339.
- (48) Minomura, S. *J. Phys. Colloq.* **1981**, *42*, 181-188.
- (49) Koch-Müller, M.; Rhede, D.; Schulz, R.; Wirth, R. **2009**, *Phys. Chem. Min.* *36*, 329-341.
- (50) Akaogi, M.; Yusa, H.; Shiraishi, K.; Suzuki, T. **1995**, *J. Geophys. Res.* *100*, 337 - 347.
- (51) Morishima, H.; Kato, T.; Suto, M.; Ohtani, E.; Urakawa, S.; Utsumi, W.; Shimomura, O.; Kikegawa, T. *Science* **1994**, *26*, 1202 - 1203.
- (52) Inoue, T.; Irifune, T.; Higo, Y.; Sanehira, T.; Sueda, Y.; Yamada, A.; Shinmei, T.; Yamazaki, D.; Ando, J.; Funakoshi, K.; Utsumi, W. *Phys. Chem. Min.* **2006**, *33*, 106-114.
- (53) Gasparik, T., *Contr. Min. Petr.* **1989**, *102*, 389 - 405.
- (54) Goldstein, J. I.; Newbury, D. E.; Echlin, P. *Scanning Electron Microscopy and X-ray Microanalysis*; Plenum Press, New York, **1992**.
- (55) McGaff, A. J.; Serghiou, G.; Frost, D. J. *High Pressure Res.* **2008**, *28*, 491-495.
- (56) Vincent, R.; Midgley, P. A. *Ultramicroscopy* **1994**, *53*, 271-282.
- (57) Morniroli, J. P.; Auchterlonie, G. J.; Drennan, J.; Zou, J. *J. Microsc.* **2008**, *232*, 7-26.
- (58) Morniroli, J. P.; Ji, G. **2009**, *Mat. Res. Soc. Symp. Proc.* *1184*, 37-48.
- (59) Ji, G.; Morniroli, J. P.; Aucherlonie, G. J.; Drnnan, J.; Jacob, D. *Ultramicroscopy* **2009**, *109*, 1282-1294.
- (60) Morniroli, J. P.; Ji, G.; Jacob, D. *Ultramicroscopy* **2012**, *121*, 42-60.
- (61) Jacob, D.; Ji, G.; Morniroli, J. P. *Ultramicroscopy* **2012**, *121*, 61-71.
- (62) Ji, G.; Morniroli, J. P. *J. Appl. Cryst.* **2013**, *46*, 430-442.
- (63) Hadermann, J.; Abakumov, A. M.; Turner, S.; Hafideddine, Z.; Khasanova, N. R.; Antipov, E. V.; Van Tendeloo, G. *Chem. Mater.* **2011**, *23*, 3540-3545.
- (64) Vaughan, G. B. M.; Wright, J. P.; Bytchkov, A.; Rossat, H.; Gleyzolle, I.; Snigireva, I.; Snigirev, A. *J. Synchr. Radiat.* **2011**, *30*, 125-133.
- (65) Morniroli, J. P.; *Electron Diffraction 7.01 LMPGM UMR CNRS 8517*, France, 2004.
- (66) Hammersley, A. P.; Svensson, S.O.; Hanfland, M.; Fitch, A. N.; Hausermann, D. *High Pressure Res.* **1996**, *14*, 235-248.
- (67) Bruker AXS, TOPAS (Bruker AXS inc, Karlsruhe, Germany, 2006).
- (68) Solé, V. A.; Papillon, E.; Cotte, M.; Walter, Ph.; Susini, J., *Spectrochim. Acta Part B* **2007**, *62*, 63-68.
- (69) Crain, J.; Ackland, G. J.; Clark, S. J. *Rep. Prog. Phys.* **1995**, *58*, 705-754.
- (70) Queisser, G.; Grosshans, W. A.; Holzapfel, W. B. *Europhys. Lett.* **1987**, *3*, 1109-1112.

- (71) Lv, M. Y.; Chen, Z. W.; Liu, R. P.; Wang, W. K. *Solid State Comm.* **2005**, *135*, 749-752.
- (72) Werner, A.; Sanjuro, J. A.; Cardona, M. *Solid State Comm.* **1982**, *44*, 155-158.
- (73) Soma, T.; Iwanami, H.; Matsuo, H. *Solid State Commun.* **1982**, *42*, 469-471.
- (74) da Silva, CRS; Venezuela, P; da Silva, A. J. R.; Fazzio, A. *Solid State Comm.* **2001**, *120*, 369-373.
- (75) Hao, A.; Zhang, L.; Gao, Z.; Zhu, Y.; Liu, R. P. *Phys. Stat. Sol. B-Basic Solid State Phys.* **2011**, *248*, 1135-1138.
- (76) Wang, Jian-Tao; Chen, C.; Mizuseki, H.; Kawazoe, Y. *Phys. Rev. Lett.* **2013**, *110*, 165503-166508.
- (77) Clark, S. J.; Ackland, G. J.; Crain, J. *Phys. Rev. B* **1994**, *49*, 5341-5352.
- (78) Nelmes, R. J.; McMahon, M. I.; Wright, N. G.; Allan, D. R.; Loveday, J. S. *Phys. Rev. B* **1993**, *48*, 9883-9886.
- (79) Guillaume, C.; Serghiou, G.; Thomson, A.; Morniroli, J. P.; Frost, D. J.; Odling, N.; Mezouar, M. *J. Am. Chem. Soc.* **2009**, *131*, 7550-7551.
- (80) Hull, S.; Keen, D. A. *Phys. Rev. B* **1994**, *50*, 5868-5885.
- (81) Lambrecht, W. R. L.; Amador, C.; Segall, B. *Phys. Rev. Lett.* **1992**, *68*, 1363-1366.
- (82) Guillaume, C. L.; Serghiou, G.; Thomson, A.; Morniroli, J. P.; Frost, D. J.; Odling, N. ; Jeffree, C. E. *Inorg. Chem.* **2010**, *49*, 8230-8236.
- (83) Serghiou, G.; Guillaume, C. L.; Jeffree, C. E.; ; Thomson, A.; Frost, D. J.; Morniroli, J. P.; Odling, N. *High Pressure Res.* **2010**, *30*, 44-50.

Table of contents synopsis



Pressure gently tunes to radically transforms matter, making it formidable in developing targeted materials and materials landscapes. Crystals may initially be small and sparsely populated within complex agglomerates. X-ray and electron diffraction offer complementing angular and spatial resolution. Precession improves electron diffraction intensities, strengthening single-crystal assignment. We develop a dense SiGe landscape by heating Si and Ge at pressures where they undergo phase transitions, transform to metals and their melting points converge. Distinctive precession electron diffraction patterns are shown above.